

Non-Abelian properties of electron wave packets in Dirac semimetals A_3Bi ($A=Na,K,Rb$)

E. V. Gorbar,^{1,2} V. A. Miransky,³ I. A. Shovkovy,^{4,5} and P. O. Sukhachov³

¹*Department of Physics, Taras Shevchenko National Kiev University, Kiev, 03680, Ukraine*

²*Bogolyubov Institute for Theoretical Physics, Kiev, 03680, Ukraine*

³*Department of Applied Mathematics, Western University, London, Ontario, Canada N6A 5B7*

⁴*College of Integrative Sciences and Arts, Arizona State University, Mesa, Arizona 85212, USA*

⁵*Department of Physics, Arizona State University, Tempe, Arizona 85287, USA*

(Dated: July 30, 2018)

The motion of electron wave packets in the Dirac semimetals A_3Bi ($A=Na,K,Rb$) is studied in a semiclassical approximation. Because of the two-fold degeneracy of the Dirac points and a momentum-dependent gap term in the low-energy Hamiltonian, the associated Berry curvature is non-Abelian. In the presence of background electromagnetic fields, such a Berry curvature leads to a splitting of trajectories for the wave packets that originate from different Dirac points and chiral sectors. The nature of the splitting strongly depends on the background fields as well as the initial chiral composition of the wave packets. In parallel electric and magnetic fields, while a well-pronounced valley splitting is achieved for any chirality composition, the chirality separation takes place predominantly for the initially polarized states. On the other hand, in perpendicular electric and magnetic fields, there are clear deviations from the conventional Abelian trajectories, albeit without a well-pronounced valley splitting.

I. INTRODUCTION

Dirac and Weyl semimetals are condensed matter materials whose low-energy excitations are described by the Dirac and Weyl equations, respectively. Generically, the corresponding materials have a band structure where the valence and conduction bands touch at isolated points (i.e., the Dirac points and the Weyl nodes, respectively). Theoretically, A_3Bi ($A=Na,K,Rb$) and Cd_3As_2 were the first compounds predicted to be Dirac semimetals with topologically protected Dirac points [1, 2]. The existence of Dirac points in Cd_3As_2 and Na_3Bi was soon confirmed experimentally via the angle-resolved photoemission spectroscopy (ARPES) in Refs. [3–5]. Weyl semimetals were first predicted in pyrochlore iridates [6], but they were discovered experimentally in TaAs, TaP, NbAs, and NbP [7–16] (for recent reviews, see Refs. [17–19]).

As it is well understood now, Weyl semimetals represent a topologically nontrivial phase of matter. Indeed, Weyl nodes are the monopoles of the Berry curvature [20] whose topological charges are directly connected with their chirality. According to the Nielsen–Ninomiya theorem [21, 22], Weyl nodes in crystals always come in pairs of opposite chirality. The corresponding nodes are separated in momentum and/or energy. Such a nodal structure is also responsible for the existence of topologically protected surface states, known as the Fermi arcs [6, 23, 24].

Unlike the Weyl nodes, the Dirac points are usually assumed to be topologically trivial because they are composed from pairs of overlapping Weyl nodes of opposite chirality. By using numerical calculations [1, 2], however, it was found that the Dirac semimetals Cd_3As_2 and A_3Bi ($A=Na,K,Rb$) possess the Fermi arcs too. This was later confirmed experimentally by the ARPES data [25] and the observation of special surface-bulk quantum oscillations in transport measurements [26, 27]. It was argued [28–34] that the physical reason for the nontrivial topological properties of A_3Bi ($A=Na,K,Rb$) is a Z_2 symmetry that such materials possess. In the classification scheme proposed in Ref. [28], such Dirac semimetals belong to the second class in which pairs of Dirac points are created by the inversion of two bands. This is in contrast to the Dirac semimetals in the first class that possess a single Dirac point at a time-reversal (TR) invariant momentum. As noted in Ref. [34], the presence of the Z_2 symmetry leads to the Z_2 anomaly that could affect transport properties. The latter were recently discussed in Ref. [35] using the hydrodynamic description. A complementary view at the Z_2 symmetry in A_3Bi ($A=Na,K,Rb$) was presented in Refs. [29, 30], where we argued that these compounds are, in fact, hidden Z_2 Weyl semimetals. The discrete symmetry of the low-energy effective Hamiltonian allows one to split all quasiparticle states into two separate sectors, each describing a Weyl semimetal with a pair of Weyl nodes and a broken TR symmetry. Since the Z_2 symmetry interchanges states from these two sectors, the TR symmetry is preserved in the complete theory.

The degeneracy of opposite chirality states in the Dirac semimetals and the presence of the Z_2 symmetry are expected to have profound consequences. The fact that the Berry curvature becomes a matrix with a non-Abelian structure [36] could manifest itself, for example, in unusual transport properties of the Dirac semimetals. The latter could be studied, for example, by employing the chiral kinetic theory [37–40] generalized to the case of degenerate states [41–44].

The main motivation for this study is to investigate how the momentum-dependent gap term and the non-Abelian nature of the Berry curvature affect the quasiclassical properties of electron wave packets in Z_2 Weyl semimetals. In particular, we consider the propagation of wave packets in external electric and magnetic fields. Note that, in the absence of the non-Abelian corrections to the Berry curvature, the semiclassical motion of chiral quasiparticles was already considered in Ref. [45], where the (pseudo-)magnetic lens was proposed. It was found that while the primary contribution to the spatial splitting of quasiparticles of different chirality is related to the interplay of magnetic and strain-induced pseudomagnetic fields, the Abelian Berry curvature plays also an important, albeit auxiliary, role. In this study, we investigate how the trajectories of the wave packets change due to the presence of the off-diagonal gap term and the non-Abelian nature of the Berry curvature. Of particular interest is the question as to whether the splitting of the wave packets from different Dirac points (or, equivalently, valleys) and different chiral sectors can be achieved without a background pseudomagnetic field.

The paper is organized as follows. In Sec. II, the low-energy effective model of the Dirac semimetals A_3Bi ($A=Na,K,Rb$) and its linearized version are introduced. We present the semiclassical equations of motion with the non-Abelian corrections in Sec. III. The motion of the electron wave packets in external electric and magnetic fields is investigated in Sec. IV. The results are discussed and summarized in Sec. V. The expressions for the Berry connection, the Berry curvature, and the magnetic moment of wave packets are given in Appendix A.

II. MODEL

In this section, we describe the low-energy model of the Dirac semimetals A_3Bi ($A=Na,K,Rb$) as well as its linearized version and underlying symmetries. The corresponding quasiparticle Hamiltonian derived in Ref. [1] reads as

$$H(\mathbf{k}) = \epsilon_0(\mathbf{k})I_4 + H_{4 \times 4}, \quad (1)$$

where I_4 is the 4×4 unit matrix, $\epsilon_0(\mathbf{k}) = C_0 + C_1k_z^2 + C_2k_\perp^2$, $k_\perp = \sqrt{k_x^2 + k_y^2}$, and

$$H_{4 \times 4} = \begin{pmatrix} M(\mathbf{k}) & v_F k_+ & 0 & \Delta^*(\mathbf{k}) \\ v_F k_- & -M(\mathbf{k}) & \Delta^*(\mathbf{k}) & 0 \\ 0 & \Delta(\mathbf{k}) & M(\mathbf{k}) & -v_F k_- \\ \Delta(\mathbf{k}) & 0 & -v_F k_+ & -M(\mathbf{k}) \end{pmatrix}. \quad (2)$$

The matrix Hamiltonian $H_{4 \times 4}$ is naturally split into 2×2 blocks. The diagonal blocks are defined in terms of the quadratic function $M(\mathbf{k}) = M_0 - M_1k_z^2 - M_2k_\perp^2$ and $v_F k_\pm$, where $k_\pm = k_x \pm ik_y$. The off-diagonal blocks are determined by the function $\Delta(\mathbf{k}) = \alpha k_z k_\pm^2$ that plays a crucial role in this study and whose physical meaning will be discussed later.

The numerical values of parameters in Hamiltonian (1) can be determined by fitting the energy spectrum obtained by the first-principles calculations [1] and equal

$$\begin{aligned} C_0 &= -0.06382 \text{ eV}, & C_1 &= 8.7536 \text{ eV } \text{\AA}^2, & C_2 &= -8.4008 \text{ eV } \text{\AA}^2, \\ M_0 &= -0.08686 \text{ eV}, & M_1 &= -10.6424 \text{ eV } \text{\AA}^2, & M_2 &= -10.3610 \text{ eV } \text{\AA}^2, \\ v_F &= 2.4598 \text{ eV } \text{\AA}. \end{aligned} \quad (3)$$

Note that the Fermi velocity v_F is given in energy units. Since no specific value for α , which determines the magnitude of the off-diagonal terms, was quoted in Ref. [1], we will treat it as a free, albeit small, parameter below. In addition to the model parameters in Eq. (3), we will also need the transport scattering time τ . For the purposes of this study, we use $\tau \approx 10^{-10}$ s, which is an estimated value of the scattering time in Cd_3As_2 [46].

The energy eigenvalues of Hamiltonian (1) are given by the following expression:

$$\epsilon(\mathbf{k}) = \epsilon_0(\mathbf{k}) \pm \sqrt{M^2(\mathbf{k}) + v_F^2 k_\perp^2 + |\Delta(\mathbf{k})|^2}. \quad (4)$$

As is clear, a nonzero $\epsilon_0(\mathbf{k})$ introduces an asymmetry between the positive (electrons) and negative (holes) energy branches and, consequently, breaks the particle-hole symmetry. The square root term vanishes at the two Dirac points, $\mathbf{k}_0^{(\pm)} = (0, 0, \pm\sqrt{m})$, where $\sqrt{m} = \sqrt{M_0/M_1}$. By using the low-energy parameters in Eq. (3), we find that $\sqrt{m} \approx 0.0903 \text{ \AA}^{-1}$. The latter defines the characteristic momentum scale in the low-energy Hamiltonian. Therefore, by equating the last two terms under the square root in Eq. (4) and setting $k_z = k_\perp = \sqrt{m}$, we can estimate the characteristic value of parameter α , i.e.,

$$\alpha^* = \frac{v_F}{m} \approx 301.384 \text{ eV } \text{\AA}^3. \quad (5)$$

In order to get a better insight into the role of the off-diagonal term in the low-energy Hamiltonian, we plot the corresponding energy spectra for $\alpha = 0$ and $\alpha = 10\alpha^*$ in the two panels of Fig. 1. As expected from Eq. (4), there are two Dirac points well separated in k_z . The term $\Delta(\mathbf{k})$ plays the role of a momentum-dependent gap function that mixes eigenstates of opposite chirality. While $\Delta(\mathbf{k})$ can profoundly change the spectrum of quasiparticles for sufficiently large k_\perp , it vanishes at the Dirac points. Thus, the upper and lower 2×2 blocks of Hamiltonian (2) still describe quasiparticle states of opposite chirality in a sufficiently close vicinity of the Dirac points, although, strictly speaking, the notion of chirality is rigorous only at $\alpha = 0$.

As discussed in detail in Refs. [29, 30], the actual form of function $\Delta(\mathbf{k})$ is consistent with the discrete Z_2 symmetry, implying that the Dirac semimetals $A_3\text{Bi}$ ($A=\text{Na}, \text{K}, \text{Rb}$) are effectively the hidden Z_2 Weyl semimetals. The quasiparticle states of these materials can be naturally split by using the ud (up-down) symmetry [29]

$$U_\chi = \Pi_{k_z \rightarrow -k_z} \begin{pmatrix} I_2 & 0 \\ 0 & -I_2 \end{pmatrix}, \quad (6)$$

where $\Pi_{k_z \rightarrow -k_z}$ is the operator that changes the sign of the z component of momentum and I_2 is the 2×2 unit matrix. The TR symmetry is broken in each of the Z_2 sectors that signifies the presence of the Weyl semimetal phase with the Weyl nodes separated by $2\sqrt{m}$. Since the chirality of the nodes in different Z_2 sectors is opposite, the complete model preserves the TR symmetry and has two Dirac points.

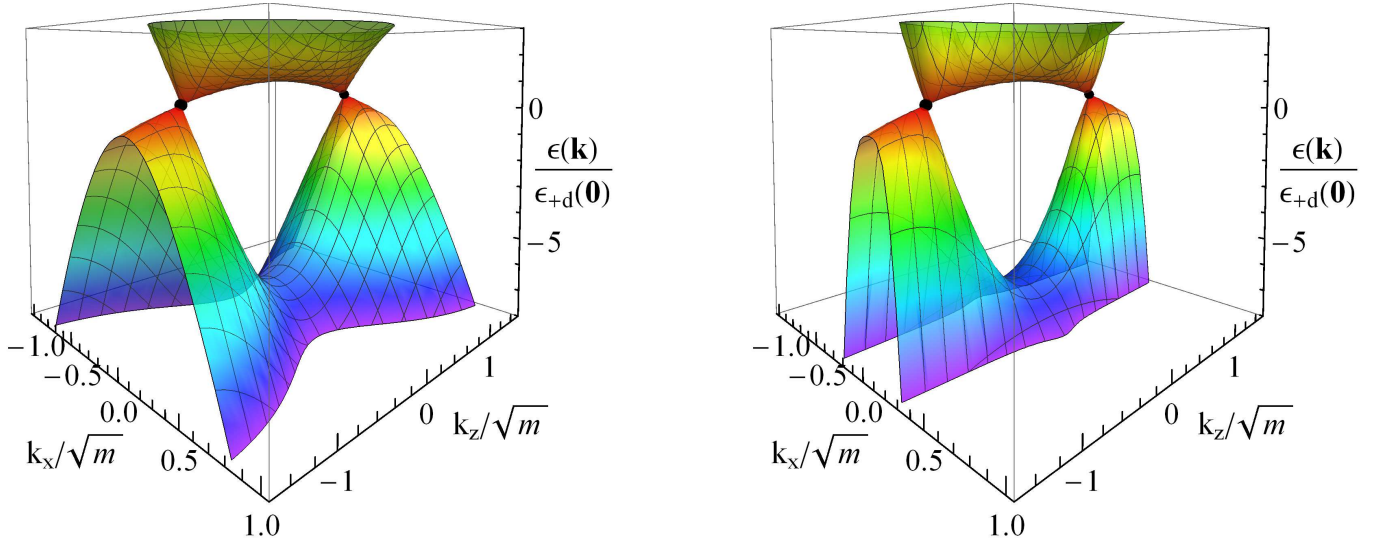


FIG. 1: The energy spectrum of the low-energy model (1) at $\alpha = 0$ (left panel) and $\alpha = 10\alpha^*$ (right panel), where α^* is the characteristic value defined in Eq. (5) and $\epsilon_{+d}(0)$ is defined in Eq. (10).

In order to simplify the calculations, we will omit the term $\epsilon_0(\mathbf{k})$ and linearize Hamiltonian (1) in the vicinity of the Dirac points $\mathbf{k}_0^{(\pm)}$. By expanding $M(\mathbf{k})$ up to the linear order in deviations $\delta\mathbf{k} = \mathbf{k} - \mathbf{k}_0^{(\pm)}$ and performing the unitary transformation with $U_x = \text{diag}(\sigma_x, I_2)$, we obtain

$$H_{\text{lin}}^{(+)}(\tilde{\mathbf{k}}) = \begin{pmatrix} v_F (\tilde{k}_x \sigma_x + \tilde{k}_y \sigma_y - \tilde{k}_z \sigma_z) & \alpha (\sqrt{m} + \tilde{k}_z) \tilde{k}_-^2 \\ \alpha (\sqrt{m} + \tilde{k}_z) \tilde{k}_+^2 & -v_F (\tilde{k}_x \sigma_x + \tilde{k}_y \sigma_y - \tilde{k}_z \sigma_z) \end{pmatrix} \quad (7)$$

in the vicinity of the Dirac point at $\mathbf{k}_0^{(+)}$ and

$$H_{\text{lin}}^{(-)}(\tilde{\mathbf{k}}) = \begin{pmatrix} v_F (\tilde{\mathbf{k}} \cdot \boldsymbol{\sigma}) & -\alpha (\sqrt{m} - \tilde{k}_z) \tilde{k}_-^2 \\ -\alpha (\sqrt{m} - \tilde{k}_z) \tilde{k}_+^2 & -v_F (\tilde{\mathbf{k}} \cdot \boldsymbol{\sigma}) \end{pmatrix} \quad (8)$$

in the vicinity of the Dirac point at $\mathbf{k}_0^{(-)}$. Here $\boldsymbol{\sigma}$ are the Pauli matrices and $\tilde{\mathbf{k}} = (k_x, k_y, 2\sqrt{M_0 M_1} \delta k_z / v_F)$. In the model at hand $2\sqrt{M_0 M_1} \approx 0.78 v_F$ and, consequently, the quasiparticle energy spectra near the Dirac points can

be approximately considered as isotropic $\tilde{\mathbf{k}} = (k_x, k_y, \delta k_z)$. The corresponding positive branches of the energies for Hamiltonians (7) and (8) are given by

$$\epsilon^{(\pm)}(\tilde{\mathbf{k}}) = \sqrt{v_F^2 \tilde{k}^2 + \alpha^2 (\sqrt{m} \pm \tilde{k}_z)^2} k_\perp^2, \quad (9)$$

where the superscript labels the Dirac points at $\mathbf{k}_0^{(\pm)}$. Note that we keep the \tilde{k}_z term in the off-diagonal components in Eqs. (7) and (8) because, as will be clear below, it is relevant for the Berry connection and the magnetic moment, which contain derivatives with respect to the z component of momentum. Also, this term plays an important role in determining the wave packet velocity.

Obviously, the dynamics of quasiparticles can be reliably described in terms of the two independent linearized Hamiltonians (7) and (8) only for sufficiently small energies and deviations of momentum, $|\delta k_z| \lesssim \sqrt{m}$. The constraint $|\delta k_z| \lesssim \sqrt{m}$ also ensures that the internode transitions are negligible. In order to obtain the characteristic energy scales of the low-energy region, we calculate the height of the energy “domes” in the full Hamiltonian (1) at $\mathbf{k} = \mathbf{0}$, see also Fig. 1. The corresponding values read as

$$\epsilon_{+d}(0) = 23.0 \text{ meV}, \quad \epsilon_{-d}(0) = -150.7 \text{ meV} \quad (10)$$

for positive and negative energies, respectively. Without the term $\epsilon_0(\mathbf{k})$, we have

$$\epsilon_{+d}(0)|_{\epsilon_0=0} = -\epsilon_{-d}(0)|_{\epsilon_0=0} = 86.9 \text{ meV}. \quad (11)$$

In order to simplify our notations, in the following we assume that the momentum \mathbf{k} is measured from the corresponding Dirac points, i.e., we replace δk_z with k_z .

The energy spectrum (9) at each Dirac point is doubly degenerate in energy with the corresponding wave functions given by

$$\psi_{+, \mathbf{k}}^{(\pm)} = \frac{v_F k_\perp}{\sqrt{[\epsilon^{(\pm)}(\mathbf{k}) \pm v_F k_z]^2 + v_F^2 k_\perp^2 + \alpha^2 (k_z \pm \sqrt{m})^2 k_\perp^2}} \begin{pmatrix} 1 \\ \frac{\epsilon^{(\pm)}(\mathbf{k}) \pm v_F k_z}{v_F k_-} \\ 0 \\ \frac{\alpha(k_z \pm \sqrt{m}) k_\perp^2}{v_F k_-} \end{pmatrix}, \quad (12)$$

$$\psi_{-, \mathbf{k}}^{(\pm)} = \frac{v_F k_\perp}{\sqrt{[\epsilon^{(\pm)}(\mathbf{k}) \mp v_F k_z]^2 + v_F^2 k_\perp^2 + \alpha^2 (k_z \pm \sqrt{m})^2 k_\perp^2}} \begin{pmatrix} 0 \\ \frac{\alpha(k_z \pm \sqrt{m}) k_\perp^2}{v_F k_-} \\ 1 \\ -\frac{\epsilon^{(\pm)}(\mathbf{k}) \mp v_F k_z}{v_F k_-} \end{pmatrix}. \quad (13)$$

Here the upper index corresponds to the Dirac points at $\mathbf{k}_0^{(\pm)}$, which are described by the linearized Hamiltonians (7) and (8), respectively. As we will see below, this degeneracy is responsible for the non-Abelian nature of the Berry curvature in the Dirac semimetals $A_3\text{Bi}$ ($A=\text{Na, K, Rb}$). It also implies that the semiclassical equations of motion for a degenerate case [41–44] should be used. In order to describe this degeneracy, we introduce the following transformation that can be viewed as an analog of the discrete chiral symmetry:

$$\Gamma_5 = \Pi_{\alpha \rightarrow -\alpha} \begin{pmatrix} I_2 & 0 \\ 0 & -I_2 \end{pmatrix}. \quad (14)$$

Note that Γ_5 is not a true symmetry because it does not commute with the linearized Hamiltonians (7) and (8). The wave functions $\psi_{+, \mathbf{k}}^{(\pm)}$ and $\psi_{-, \mathbf{k}}^{(\pm)}$ are the eigenstates of Γ_5 , i.e., $\Gamma_5 \psi_{+, \mathbf{k}}^{(\pm)} = \psi_{+, \mathbf{k}}^{(\pm)}$ and $\Gamma_5 \psi_{-, \mathbf{k}}^{(\pm)} = -\psi_{-, \mathbf{k}}^{(\pm)}$, that describe the states with the positive and negative chirality, respectively, in the limit $\alpha \rightarrow 0$. In addition, the positive branch of the band energy for the linearized Hamiltonians (7) and (8) is

$$\epsilon^{(+)}(\mathbf{k}) = \sqrt{v_F^2 k^2 + \alpha^2 (\sqrt{m} \pm k_z)^2} k_\perp^2 \approx v_F k + O(\alpha^2). \quad (15)$$

Henceforth, we will consider only the electron wave packets with positive energies.

III. NON-ABELIAN CORRECTIONS TO THE EQUATIONS OF MOTION

In this section, we consider the electron wave packets in the Z_2 Weyl semimetals and present the corresponding equations of motion. Since we treat the Dirac points as independent and, consequently, there are no internode mixing terms, the superscript \pm for all quantities will be omitted in this section. An electron wave packet centered at $\mathbf{r}(t)$ and $\mathbf{q}(t)$ is defined as a superposition of the Bloch states $\phi_{n,\mathbf{k}} = e^{i\mathbf{k}\mathbf{r}}\psi_{n,\mathbf{k}}$, i.e.,

$$W = \sum_{n=\pm} \int \frac{d\mathbf{k}}{(2\pi)^3} a(t, \mathbf{k}) \eta_n(t, \mathbf{k}) \phi_{n,\mathbf{k}}. \quad (16)$$

Here $n = \pm$ denotes the degenerate chiral states and $a(t, \mathbf{k})$ is a normalized distribution centered at $\mathbf{r}(t)$ and $\mathbf{q}(t)$. Finally, $\eta_n(t, \mathbf{k})$ denotes the partial contributions or weights of the degenerate states, satisfying the normalization condition $\sum_{n=\pm} |\eta_n(t, \mathbf{k})|^2 = 1$.

As is well known, the nontrivial topological properties of Weyl semimetals are captured by the monopole-like Berry curvature [20] at the Weyl nodes. Because of the additional Γ_5 -chirality degree of freedom at each Dirac point in the $A_3\text{Bi}$ ($A=\text{Na, K, Rb}$) semimetals, the corresponding Berry connection is a 2×2 matrix. Its elements are defined by

$$\mathbf{A}_{nm}(\mathbf{q}) = -\frac{i}{2} (\psi_{n,\mathbf{q}}^\dagger \partial_{\mathbf{q}} \psi_{m,\mathbf{q}} - \psi_{m,\mathbf{q}}^\dagger \partial_{\mathbf{q}} \psi_{n,\mathbf{q}}). \quad (17)$$

The explicit expressions for \mathbf{A}_{nm} are given by Eqs. (A1)–(A4) in Appendix A. (Note that the off-diagonal components of \mathbf{A}_{nm} vanish when $\alpha = 0$.) The Berry curvature has a non-Abelian structure, i.e.,

$$\boldsymbol{\Omega}_{nm}(\mathbf{q}) = -\frac{i}{\hbar} \sum_{l=\pm} [(D_{\mathbf{q}})_{nl} \times (D_{\mathbf{q}})_{lm}] = \frac{1}{\hbar} [\partial_{\mathbf{q}} \times \mathbf{A}_{nm}(\mathbf{q})] + \frac{i}{\hbar} \sum_{l=\pm} [\mathbf{A}_{nl}(\mathbf{q}) \times \mathbf{A}_{lm}(\mathbf{q})], \quad (18)$$

where $(D_{\mathbf{q}})_{nl} = \partial_{\mathbf{q}} \delta_{nl} + i\mathbf{A}_{nl}(\mathbf{q})$ is the covariant derivative. The components of $\boldsymbol{\Omega}_{nm}(\mathbf{q})$ are given by Eqs. (A5)–(A8) in Appendix A. The semiclassical Hamiltonian is defined by

$$\mathcal{H}_{nm}(\mathbf{r}, \mathbf{q}) = [\epsilon(\mathbf{q}) - e\varphi(\mathbf{r})] \delta_{nm} + (\mathbf{M}_{nm}(\mathbf{q}) \cdot \mathbf{B}) \quad (19)$$

and contains the band, electrostatic, as well as the magnetization energy determined by the magnetic moment of the wave packet, i.e.,

$$\mathbf{M}_{nm}(\mathbf{q}) = i \frac{e}{2\hbar c} [(\partial_{\mathbf{q}} \psi_{n,\mathbf{q}}^\dagger) \times \{H(\mathbf{q}) - \epsilon(\mathbf{q}) I_2\} (\partial_{\mathbf{q}} \psi_{m,\mathbf{q}})]. \quad (20)$$

Here $H(\mathbf{q})$ is given by $H_{\text{lin}}^{(\pm)}(\mathbf{q})$ in Eqs. (7) and (8) for the Dirac points at $\mathbf{k}_0^{(\pm)}$, respectively, and the band energy $\epsilon(\mathbf{q})$ is defined by Eq. (9). The explicit expressions for the components of the magnetic moment (20) are given by Eqs. (A9)–(A12) in Appendix A.

The equations of motion for the non-Abelian wave packet in constant external electric \mathbf{E} and magnetic \mathbf{B} fields are given by [42]

$$\dot{\mathbf{r}} = \mathbf{v}(\mathbf{q}) + \hbar [\dot{\mathbf{q}} \times \boldsymbol{\Omega}(\mathbf{q})], \quad (21)$$

$$\hbar \dot{\mathbf{q}} = -e\mathbf{E} - \frac{e}{c} [\dot{\mathbf{r}} \times \mathbf{B}] - \frac{\hbar \mathbf{q}}{\tau}, \quad (22)$$

$$i\hbar \dot{\eta}_n = [(\mathbf{M}_{nm}(\mathbf{q}) \cdot \mathbf{B}) + \hbar (\dot{\mathbf{q}} \cdot \mathbf{A}_{nm}(\mathbf{q}))] \eta_m, \quad (23)$$

where the wave packet's velocity is defined by

$$\begin{aligned} \mathbf{v}(\mathbf{q}) &= \frac{1}{\hbar} \sum_{n,m,l=\pm} \eta_n^\dagger [(D_{\mathbf{q}})_{nl}, \mathcal{H}_{lm}(\mathbf{r}, \mathbf{q})] \eta_m = \frac{1}{\hbar} \partial_{\mathbf{q}} \epsilon(\mathbf{q}) \\ &+ \frac{1}{\hbar} \sum_{n,m,l=\pm} \eta_n^\dagger \{ \delta_{ln} [\partial_{\mathbf{q}} (\mathbf{M}_{nm}(\mathbf{q}) \cdot \mathbf{B})] + i [\mathbf{A}_{nl}(\mathbf{q}) (\mathbf{M}_{lm}(\mathbf{q}) \cdot \mathbf{B}) - (\mathbf{M}_{nl}(\mathbf{q}) \cdot \mathbf{B}) \mathbf{A}_{lm}(\mathbf{q})] \} \eta_m \end{aligned} \quad (24)$$

and the Berry curvature reads

$$\boldsymbol{\Omega}(\mathbf{q}) = \sum_{n,m=\pm} \eta_n^\dagger \boldsymbol{\Omega}_{nm}(\mathbf{q}) \eta_m. \quad (25)$$

It is worth noting that the non-Abelian equations of motion (21)–(23) differ from those for Abelian wave packets by the presence of an additional equation for the weights of the degenerate states η_n , i.e., Eq. (23). Note also that a phenomenological dissipative term $\hbar\mathbf{q}/\tau$ was introduced in Eq. (22). Physically, it captures the effects of scattering of the electrons on impurities, defects, and phonons in the relaxation time approximation.

The system of equations (21)–(23) can be rewritten in a more convenient form where all derivatives are grouped on the left-hand sides, i.e.,

$$\dot{\mathbf{r}} \left[1 - \frac{e}{c} (\boldsymbol{\Omega} \cdot \mathbf{B}) \right] = \mathbf{v} - e [\mathbf{E} \times \boldsymbol{\Omega}] - \frac{e}{c} \mathbf{B} (\boldsymbol{\Omega} \cdot \mathbf{v}) - \frac{\hbar [\mathbf{q} \times \boldsymbol{\Omega}]}{\tau}, \quad (26)$$

$$\hbar \dot{\mathbf{q}} \left[1 - \frac{e}{c} (\boldsymbol{\Omega} \cdot \mathbf{B}) \right] = \mathbf{F}, \quad (27)$$

$$i\hbar \dot{\eta}_n \left[1 - \frac{e}{c} (\boldsymbol{\Omega} \cdot \mathbf{B}) \right] = \sum_{m=\pm} \left\{ (\mathbf{F} \cdot \mathbf{A}_{nm}) + (\mathbf{M}_{nm} \cdot \mathbf{B}) \left[1 - \frac{e}{c} (\boldsymbol{\Omega} \cdot \mathbf{B}) \right] \right\} \eta_m. \quad (28)$$

Here we used the following the short-hand notation:

$$\mathbf{F} = -e\mathbf{E} - \frac{e}{c} [\mathbf{v} \times \mathbf{B}] + \frac{e^2}{c} \boldsymbol{\Omega} (\mathbf{E} \cdot \mathbf{B}) - \frac{\hbar\mathbf{q}}{\tau} \left[1 + \frac{e}{c} (\boldsymbol{\Omega} \cdot \mathbf{B}) \right] + \frac{e\hbar\boldsymbol{\Omega}}{c\tau} (\mathbf{q} \cdot \mathbf{B}). \quad (29)$$

For simplicity of presentation, here we omitted the arguments of $\boldsymbol{\Omega}$, \mathbf{v} , \mathbf{M}_{nm} , and \mathbf{A}_{nm} . As is easy to see, the presence of the non-Abelian corrections complicates significantly the equations of motion. As a result, the latter can be solved only numerically. The corresponding solutions for the cases of perpendicular and parallel electric and magnetic fields are discussed in the next section.

IV. WAVEPACKETS MOTION

As discussed in the previous section, the time evolution of the coordinates, momenta, and partial weights of the wave packets is described by Eqs. (26), (27), and (28). The corresponding equations should be also supplemented by the initial conditions. In view of the translation invariance of the problem, we can set without the loss of generality the initial coordinates of the wave packet to be at the origin of the coordinate system, i.e.,

$$\mathbf{r}(t=0) = \mathbf{0}. \quad (30)$$

As for the initial value of the wave packet's momentum, it is convenient to match it with the steady-state value determined by the electric field in the relaxation time approximation, i.e.,

$$\mathbf{q}(t=0) = -\frac{e\tau\mathbf{E}}{\hbar}. \quad (31)$$

Concerning the initial conditions for the partial weights η_{\pm} , it is natural to assume that the wave packets are non-chiral with respect to the Γ_5 transformation (i.e., the probabilities to find an electron in the positive and negative Γ_5 -chirality states are equal), i.e.,

$$\eta_+(t=0) = \eta_-(t=0) = \frac{1}{\sqrt{2}}. \quad (32)$$

For the sake of completeness, however, in Sec. IV C we will also consider the case of the initially polarized wave packets with

$$\eta_+(t=0) = 1, \quad \eta_-(t=0) = 0 \quad (33)$$

and

$$\eta_+(t=0) = 0, \quad \eta_-(t=0) = 1. \quad (34)$$

Let us begin our consideration with the case when the background magnetic field is absent, $\mathbf{B} = \mathbf{0}$. As is easy to see, the structure of the equations of motion (26), (27), and (28) drastically simplifies, i.e.,

$$\dot{\mathbf{r}} = \mathbf{v} - e [\mathbf{E} \times \boldsymbol{\Omega}] - \frac{\hbar [\mathbf{q} \times \boldsymbol{\Omega}]}{\tau}, \quad (35)$$

$$\hbar \dot{\mathbf{q}} = -e\mathbf{E} - \frac{\hbar\mathbf{q}}{\tau}, \quad (36)$$

$$i\hbar \dot{\eta}_n = - \sum_{m=\pm} \left(\left[e\mathbf{E} + \frac{\hbar\mathbf{q}}{\tau} \right] \cdot \mathbf{A}_{nm} \right) \eta_m. \quad (37)$$

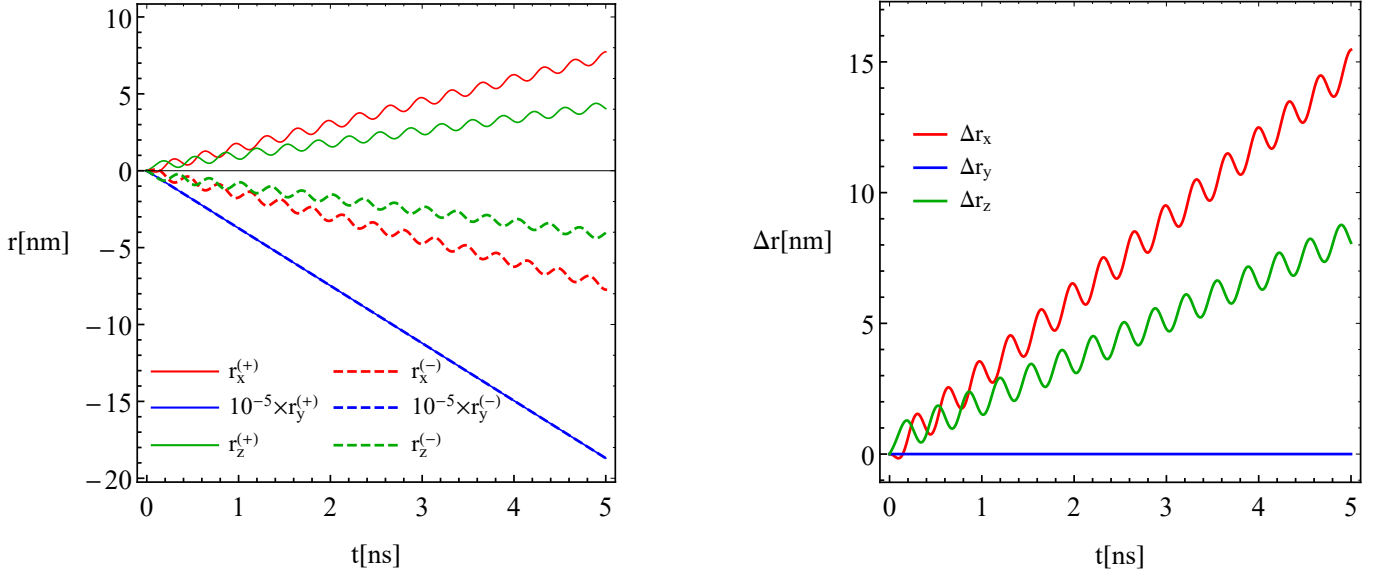


FIG. 2: The positions $\mathbf{r}^{(\pm)}$ of the wave packets as a function of time t (left panel) and the splitting $\Delta \mathbf{r} = \mathbf{r}^{(+)} - \mathbf{r}^{(-)}$ between the coordinates of the wave packets from different Dirac points (right panel). The red, blue, and green lines correspond to the x , y , and z components, respectively. The solid and dashed lines represent the results for the wave packets described by Hamiltonians (7) and (8), respectively. We used $\alpha = 0.5\alpha^*$, $\mathbf{E} = E\hat{\mathbf{y}}$, and $\mathbf{B} = B\hat{\mathbf{y}}$, where $E = 200$ V/m and $B = 10$ G.

For the initial conditions in Eqs. (30) and (31), we obtain the following analytical solution:

$$\mathbf{r}(t) = \mathbf{v}t, \quad (38)$$

$$\mathbf{q}(t) = -\frac{\tau e \mathbf{E}}{\hbar}, \quad (39)$$

$$\eta_n(t) = \eta_n(0), \quad (40)$$

which describes the inertial motion of wave packets with no mixing of the Γ_5 -chirality states. It is worth noting that this result is valid for both full and linearized Hamiltonians given in Eq. (1) as well as Eqs. (7) and (8), respectively.

As we will see below, the dynamics of wave packets becomes considerably more complicated when an external magnetic field is present. The cases of parallel and perpendicular electromagnetic fields are studied in the next two subsections.

A. Parallel electric and magnetic fields

In this subsection, we study the motion of wave packets in parallel electric and magnetic fields when the initial chiral weights are equal, i.e., $\eta_+(t=0) = \eta_-(t=0) = 1/\sqrt{2}$. In order to solve the equations of motion numerically, we set $\mathbf{E} = E\hat{\mathbf{y}}$ and $\mathbf{B} = B\hat{\mathbf{y}}$, where $E = 200$ V/m and $B = 10$ G.

The position vectors $\mathbf{r}^{(\pm)}$ of the wave packets from different valleys are shown in Fig. 2. We find that the momentum-dependent chirality-mixing leads to a noticeable splitting of the wave packets in the x and z directions that increases with time. At the same time, the splitting in the y direction is negligible. We also find that the non-Abelian terms give rise to periodic oscillations of the wave packets around their overall linear trajectories. As we argue below, the physical origin of such oscillations is connected with the precession of the magnetic moment.

Further, we find that the momenta of wave packets $\mathbf{q}^{(\pm)}$ evolve similarly to the coordinates. In particular, there is a negligible relative splitting in the y components of momenta, but the x and z components of $\mathbf{q}^{(\pm)}$ oscillate with time. Unlike the coordinates, however, the average splitting of the x and z components of momenta does not increase with time. In this connection, we should remark that the wave packet energies never exceed the threshold value (11) and, thus, the numerical analysis remains within the range of applicability of the low-energy theory.

The trajectories of the wave packets and the probabilities $|\eta_{\pm}|^2$ for the wave packets from different valleys to be in certain Γ_5 -chirality states are presented in the left and right panels of Fig. 3, respectively. The projections of trajectories onto the x - y , x - z , and y - z planes are shown in the three panels of Fig. 4. The timescale is set to

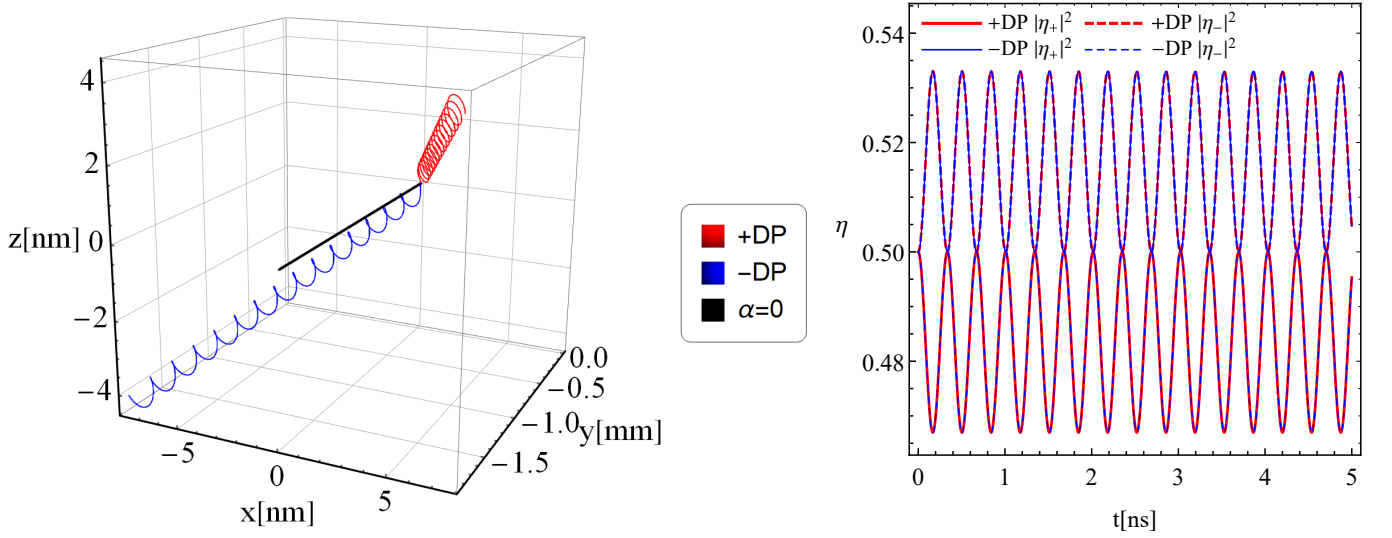


FIG. 3: Left panel: The trajectories of the wave packets from different Dirac points for $t \leq t_{\max} = 5$ ns. The red and blue lines represent the wave packets described by Hamiltonians (7) and (8) at $\alpha = 0.5\alpha^*$, respectively. The black line corresponds to the case $\alpha = 0$, where the wave packets do not split. Right panel: The time dependence of the probabilities $|\eta_{\pm}|^2$ to find the wave packets in certain Γ_5 -chirality states. The red and blue lines correspond to the wave packets described by Hamiltonians (7) and (8). The solid and dashed lines describe $|\eta_+|^2$ and $|\eta_-|^2$, respectively. We used $\mathbf{E} = E\hat{\mathbf{y}}$ and $\mathbf{B} = B\hat{\mathbf{y}}$, where $E = 200$ V/m and $B = 10$ G.

$t \leq t_{\max} = 5$ ns. In agreement with the results in Fig. 2, the trajectories for the wave packets from different Dirac points are clearly separated. The origin of the splitting of the wave packets from different valleys in the x and z directions, seen Figs. 3 and 4, can be traced back to the nontrivial structure of the low-energy Hamiltonians (7) and (8). It is remarkable that the magnitude of the average splitting linearly increases with time. By making use of this fact, we estimate that the spatial separation can reach a few micrometers for a centimeter-size crystal, provided the latter is sufficiently clean and the quasiparticle mean free path is sufficiently long. Such a splitting could provide an observational signature for the nontrivial wave packets dynamics in the Dirac semimetals $A_3\text{Bi}$ ($A=\text{Na}, \text{K}, \text{Rb}$). One should note, however, that the splitting is largely washed away in strong magnetic fields (e.g., $B = 100$ G) when the Lorentz force starts to dominate and causes the trajectories to overlap. [Note that the separation of the wave packets can be resolved experimentally only on the spatial scales larger than wave packet's characteristic sizes, i.e., $\lambda \gtrsim 2\pi/k$.]

The small spiral-like features on top of the linear separation in Fig. 4 (see also the left panel in Fig. 3) can be traced back to the oscillations of the partial weights η_{\pm} . This is also confirmed by the results for $|\eta_{\pm}|^2$ in the right panel of Fig. 3, which demonstrate that the propagation of the wave packets is accompanied by a weakly oscillating splitting of the Γ_5 -chirality. From a physics viewpoint, these oscillations are related to the precession of the magnetic moment of the wave packet. They are determined by the non-Abelian nature of the Berry curvature and the nontrivial structure of the magnetic moment. From an observational viewpoint, however, these features could be very difficult to detect. Indeed, while the oscillations could be made larger by increasing the magnetic field, the valley separation becomes weak in such a regime.

Before proceeding to the case of the perpendicular electric and magnetic fields, let us provide some underlying reasons for the spatial valley separation of wave packets. Because of a rather complicated structure of Eqs. (26), (27), and (28), we present only a rough qualitative description. To start with, we assume that the changes of the partial weights are negligible, i.e., $\eta_{\pm}(t) = \text{const.}$ In such a case, the spiral-like motion on top of the mostly linear splitting disappears. Then, it is easy to check that the remaining spatial separation is driven primarily by the velocity term in Eq. (26), i.e., the first term on the right-hand side. In fact, the separation in both x and z directions is related to the same z component of velocity \mathbf{v} . While the effect of v_z on the motion in the z direction is obvious, the splitting in the x direction is achieved indirectly. In particular, the x component of the velocity is mainly determined by the corresponding component of the momentum, which, in turn, is generated by the Lorentz force $ev_z B_y/c$ in Eq. (27), i.e., the second term in expression (29). Obviously, such a splitting is induced only when $\mathbf{B} \neq \mathbf{0}$. However, the presence of nonzero α in the energy dispersion relation (9) plays a key role as well: it gives a nonzero v_z everywhere away from the Dirac points and makes an efficient spatial separation of the wave packets possible. Thus, the valley splitting of wave packets is in large part connected with the special form of the momentum-dependent chirality-mixing term $\Delta(\mathbf{q})$ in the low-energy Hamiltonian.

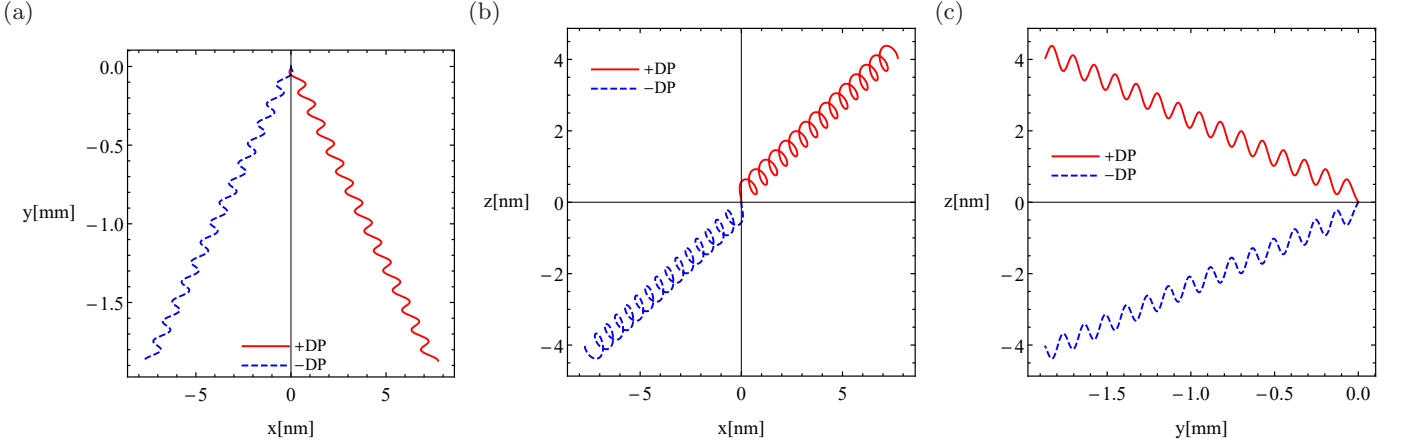


FIG. 4: The projections of the wave packet trajectories onto the following planes: x - y (panel a), x - z (panel b), and y - z (panel c). The red and blue lines correspond to the wave packets described by Hamiltonians (7) and (8), respectively. We used $t \leq t_{\max} = 5$ ns, $\alpha = 0.5\alpha^*$, $\mathbf{E} = E\hat{\mathbf{y}}$, and $\mathbf{B} = B\hat{\mathbf{y}}$, where $E = 200$ V/m and $B = 10$ G.

B. Perpendicular electric and magnetic fields

In this subsection, we consider the motion of the wave packets in perpendicular electric and magnetic fields. We use the same magnitudes of the electric and magnetic fields as in the previous subsection, but the magnetic field is now in the z direction, i.e., $\mathbf{B} = B\hat{\mathbf{z}}$. Again, $\alpha = 0.5\alpha^*$, which is sufficiently small to ensure that the relative contribution of the off-diagonal terms, quantified by $\Delta(\mathbf{q})/(v_F q)$, would remain small for the timescales used in our numerical calculations.

Let us note also that, because of the off-diagonal gap term $\propto \alpha\sqrt{m}k_{\pm}^2$, the dynamics for the two possible orientations of the magnetic field, i.e., $\mathbf{B} = B\hat{\mathbf{z}}$ and $\mathbf{B} = B\hat{\mathbf{x}}$, are not equivalent. In fact, for sufficiently large timescales, the semiclassical approximation fails in the latter case. Therefore, in this study, we will not discuss it.

The evolution of the positions $\mathbf{r}^{(\pm)}$ for the wave packets from different Dirac points (valleys) is shown in Fig. 5. As expected in the perpendicular electric and magnetic fields, the coordinates of the wave packets oscillate in the plane normal to \mathbf{B} (i.e., the x and y coordinates), albeit have a nonharmonic pattern. We also found that the non-Abelian terms lead to the oscillation-like motion of the wave packets along the z axis, as well as to a small splitting of the trajectories of the wave packets from different Dirac points (see the right panel in Fig. 5). We checked that the wave packet momenta oscillate too and split slightly when $\alpha \neq 0$. Remarkably, however, the z components of momenta vanish. We conclude, therefore, that the slow motion of the wave packets in the z direction is caused exclusively by the non-Abelian effects. In all cases presented, we verified that the energies of the wave packets remain sufficiently small to justify the use of the linearized model.

We present the trajectories of the wave packets and the probabilities $|\eta_{\pm}|^2$ to find the wave packets from different valleys in certain chiral states in the left and right panels of Fig. 6, respectively. The projections of the wave packet trajectories onto the x - y , x - z , and y - z planes are shown in the three panels of Fig. 7. The timescale is set to $t \leq t_{\max} = 0.35$ ns.

As is clear from the results in the left panel of Fig. 6, the non-Abelian corrections lead to rapid oscillations of the wave packets in the z direction. Note that while the amplitude of oscillations increases, their period decreases with time. Such a behavior suggests that the quasiclassical approximation gradually breaks down. The spatial oscillations of the wave packets can be traced back to an oscillatory time dependence of the partial weights and disappear if one enforces constant weights $\eta_{\pm}(t)$. In general, the trajectories of the wave packets from different Dirac points are asymmetric with respect to the x - y plane. On the other hand, by taking into account their substantial overlap (see the left panel of Fig. 6), we think that the valley separation cannot be easily achieved in this case. We checked, however, that trajectories change qualitatively at sufficiently large magnetic fields and the valley separation in the z direction becomes possible at least in principle, although its magnitude is estimated to be rather small.

It is interesting to point that, according to the right panel in Fig. 6, the wave packets from different Dirac points develop nonzero and opposite in sign Γ_5 -chirality polarizations. Such polarizations have an interesting oscillatory pattern with the absolute values of the partial weights reaching almost constant values at sufficiently large timescales. In summary, while the valley separation is weak, the deviation of the wave packets from the x - y plane clearly provides an evidence for the non-Abelian effects.

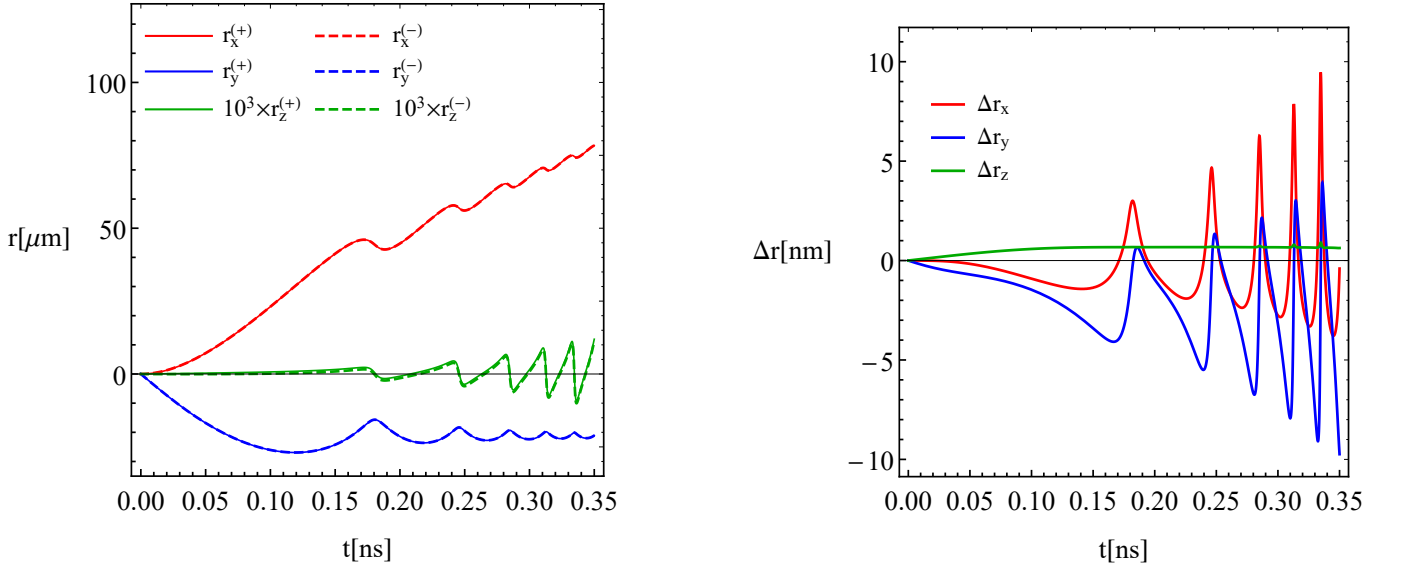


FIG. 5: The positions $\mathbf{r}^{(\pm)}$ of the wave packets as a function of time t (left panel) and the splitting $\Delta \mathbf{r} = \mathbf{r}^{(+)} - \mathbf{r}^{(-)}$ of the coordinates of the wave packets from different Dirac points (right panel). The red, blue, and green lines correspond to the x , y , and z components, respectively. The solid and dashed lines represent the results for the wave packets described by Hamiltonians (7) and (8), respectively. We used $\alpha = 0.5\alpha^*$, $\mathbf{E} = E\hat{\mathbf{y}}$ and $\mathbf{B} = B\hat{\mathbf{z}}$, where $E = 200 \text{ V/m}$ and $B = 10 \text{ G}$.

C. Motion of wave packets for chirally polarized initial states

In this subsection, for completeness, we investigate the motion of wave packets when the initial states are chirally polarized. We limit ourselves to the two limiting configurations given by Eqs. (33) and (34).

For the sake of brevity, we investigate only the most interesting case of parallel electric and magnetic fields. The corresponding results are shown in Fig. 8 with the projections onto the x - y , x - z , and y - z planes presented in the three panels of Fig. 9. The timescale is limited to $t \leq t_{\text{max}} = 1 \text{ ns}$. While the probabilities to find wave packets in states with fixed chirality are not shown, we checked that they weakly oscillate around their initial values. Just like in the case of the non-chiral wave packets discussed in Sec. IV A, the physical origin of this subdominant oscillating motion can be traced to the precession of the magnetic moment. As one can easily see from Figs. 8 and 9, the trajectories of the wave packets corresponding to different Dirac points but with the same initial Γ_5 weights are completely split and the amplitude of the splitting increases with time. On the other hand, the wave packets with different initial Γ_5 weights are weakly separated. Therefore, in the case of the nonequal initial weights (33) and (34), there is a sufficiently weak splitting of the chiral wave packets on top of the relatively large valley splitting.

V. SUMMARY AND DISCUSSIONS

In this paper, we investigated the dynamics of the electron wave packets in the Dirac semimetals A_3Bi ($\text{A}=\text{Na}, \text{K}, \text{Rb}$). We showed that due to the hidden Z_2 Weyl nature of these materials [29], the semiclassical motion of the wave packets is qualitatively affected by the non-Abelian contributions when external electric \mathbf{E} and magnetic \mathbf{B} fields are applied to the system. These contributions arise due to the degeneracy of the electron states and the chirality-mixing from $\Delta(\mathbf{k})$ in the effective Hamiltonian. Unlike the usual mass (gap) term in the Dirac Hamiltonian, $\Delta(\mathbf{k})$ is momentum-dependent and vanishes at the Dirac points. As a result, the gapless energy spectrum is preserved and the chirality remains well defined in the close vicinity of the Dirac points. The doubly degenerate states near each Dirac point can be classified with respect to the Γ_5 transformation. [Since at small $\Delta(\mathbf{k})$ the latter is approximately the same as the chiral transformation, we use the term chirality to classify the corresponding states.]

It is found that when $\mathbf{E} \parallel \mathbf{B}$ and the magnetic field is sufficiently small, the trajectories of wave packets from different valleys (or, equivalently, Dirac points) are spatially split in the plane perpendicular to the fields. What is more important, the magnitude of the valley separation grows linearly with time. One might speculate, therefore, that a substantial splitting could be achieved in macroscopic systems when the quasiparticle mean free path is sufficiently large. (Note that the propagation of wave packets depends on the relative phase of the weights whose values, however,

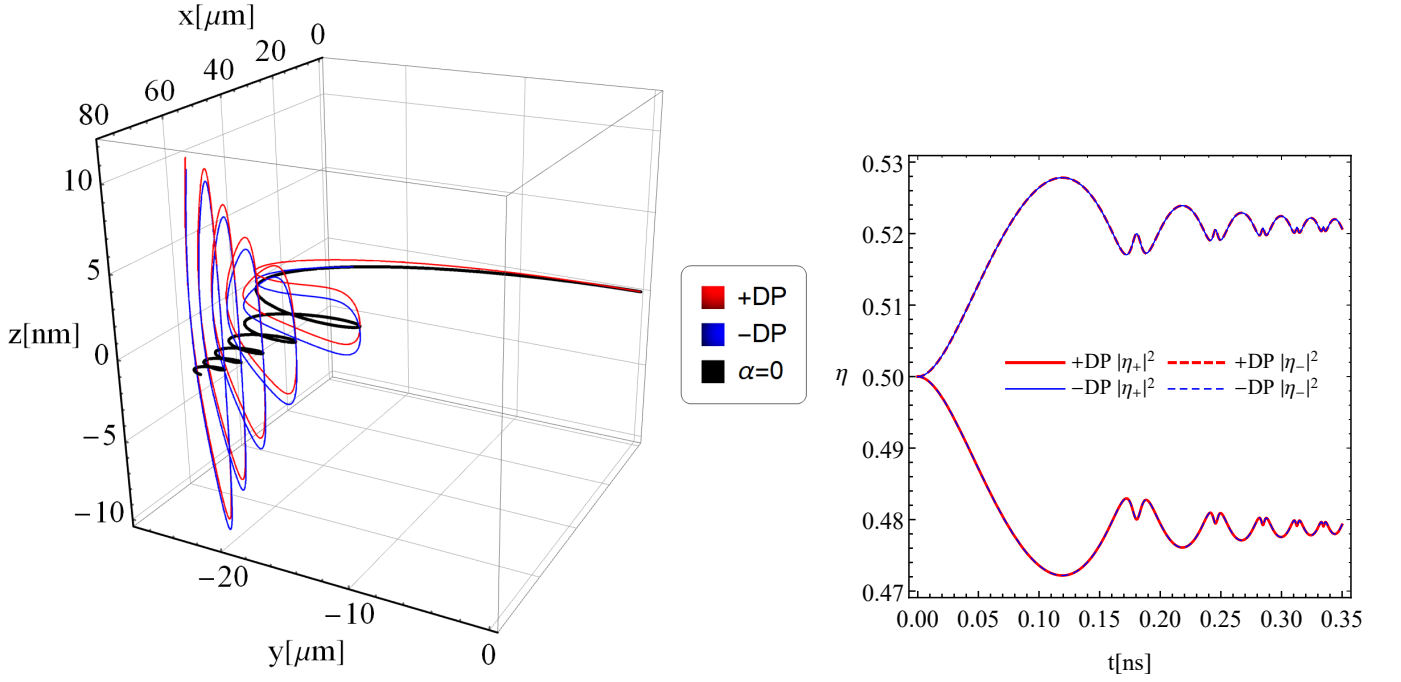


FIG. 6: Left panel: The trajectories of the wave packets corresponding to different Dirac points or valleys for $t \leq t_{\max} = 0.35$ ns. The red and blue lines represent the wave packets described by Hamiltonians (7) and (8) at $\alpha = 0.5\alpha^*$, respectively. The black line corresponds to the case $\alpha = 0$, where the wave packets are not split. Right panel: The probabilities $|\eta_{\pm}|^2$ to find the wave packets in certain Γ_5 states for $\alpha = 0.5\alpha^*$. The red and blue lines correspond to the wave packets described by Hamiltonians (7) and (8). The solid and dashed lines describe $|\eta_+|^2$ and $|\eta_-|^2$, respectively. We used $\mathbf{E} = E\hat{\mathbf{y}}$ and $\mathbf{B} = B\hat{\mathbf{z}}$, where $E = 200$ V/m and $B = 10$ G.

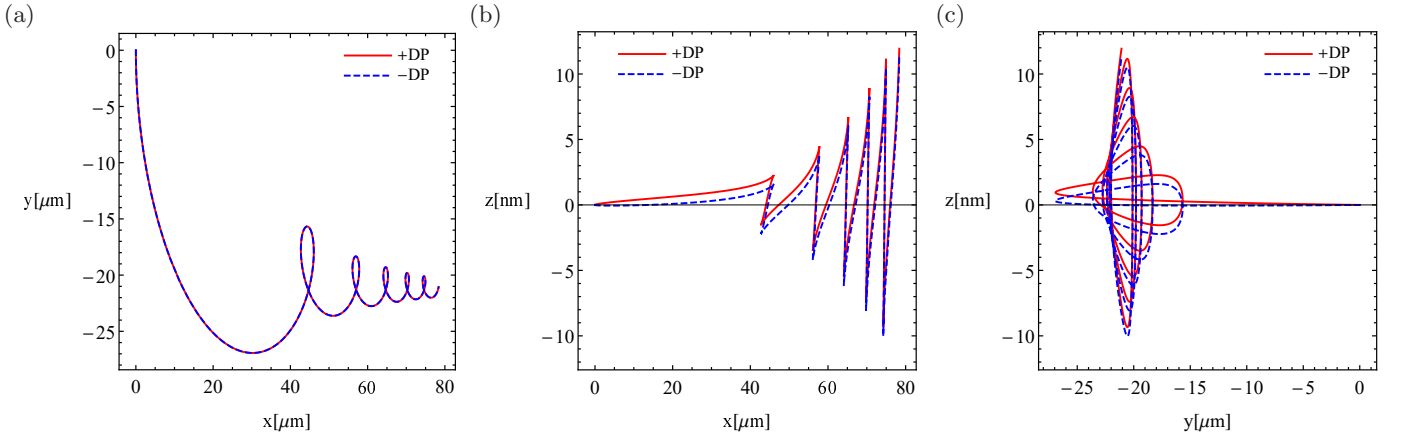


FIG. 7: The projections of the wave packets trajectories onto the following planes: x - y (panel a), x - z (panel b), and y - z (panel c). The red solid and blue dashed lines correspond to the wave packets described by Hamiltonians (7) and (8), respectively. We used $t \leq t_{\max} = 0.35$ ns, $\alpha = 0.5\alpha^*$, $\mathbf{E} = E\hat{\mathbf{y}}$, and $\mathbf{B} = B\hat{\mathbf{z}}$, where $E = 200$ V/m and $B = 10$ G.

would be difficult to control in experiments.) Interestingly, the non-Abelian corrections allow for a spiral-like motion of the wave packets on top of the almost linear separation. As is clear, the physical origin of such spiraling is connected with the precession of the magnetic moment. The same effect allows also for a small oscillating chirality polarization of the wave packets. While the amplitude of the spirals is estimated to be relatively small, the linear splitting of the trajectories due to the momentum-dependent chirality-mixing term could reach micrometers for centimeter-size crystals. When the wave packets are initially chirality polarized, there is a weak splitting of the chiral wave packets on top of the well-pronounced valley separation. The latter has the same origin as for the nonpolarized wave packets.

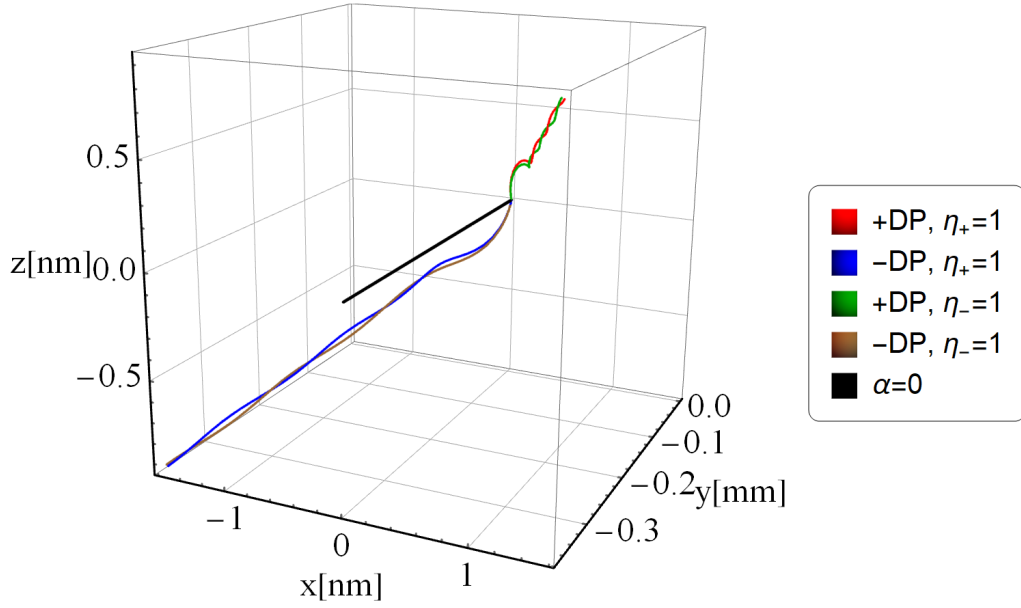


FIG. 8: The trajectories of the wave packets in parallel electric and magnetic fields. The red and blue lines correspond to the wave packets for the initial weights (33) described by Hamiltonians (7) and (8), respectively. The green and brown lines correspond to the wave packets for the initial weights (34) described by Hamiltonians (7) and (8), respectively. We used $t \leq t_{\max} = 1$ ns, $\alpha = 0.5\alpha^*$, $\mathbf{E} = E\hat{\mathbf{y}}$ and $\mathbf{B} = B\hat{\mathbf{y}}$, where $E = 200$ V/m and $B = 10$ G.

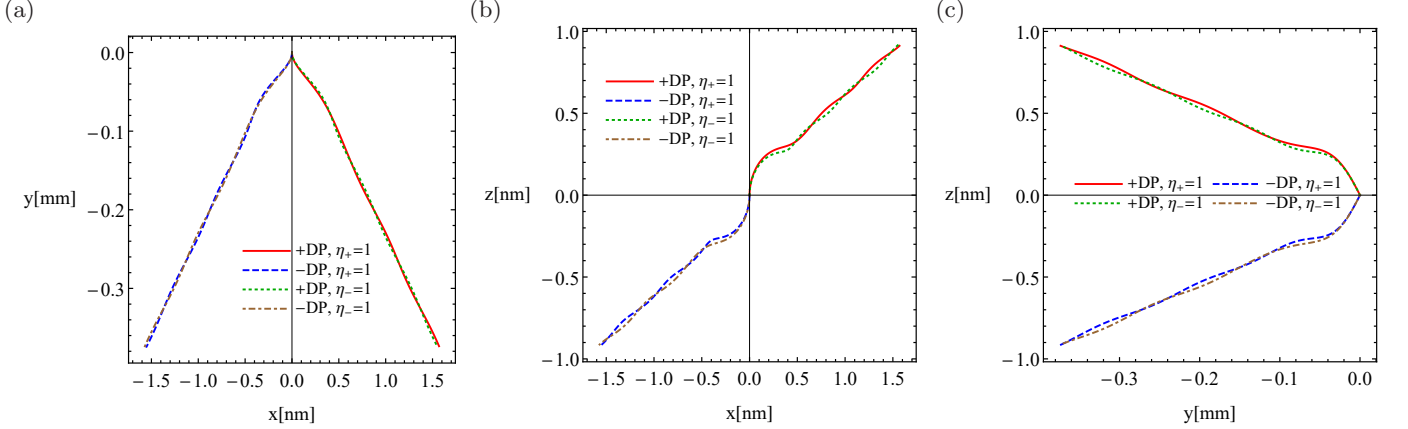


FIG. 9: The projections of the wave packet trajectories onto the following planes: x - y (panel a), x - z (panel b), and y - z (panel c). The red solid and blue dashed lines correspond to the wave packets for the initial weights (33) described by Hamiltonians (7) and (8), respectively. The green and brown lines correspond to their counterparts with the initial weights (34). We used $t \leq t_{\max} = 1$ ns, $\alpha = 0.5\alpha^*$, $\mathbf{E} = E\hat{\mathbf{y}}$ and $\mathbf{B} = B\hat{\mathbf{y}}$, where $E = 200$ V/m and $B = 10$ G.

In the case of a strong magnetic field, the Lorentz force dominates that leads to weakly separated trajectories of the wave packets from different Dirac points. Therefore, we believe that the setup with the parallel electric and magnetic fields allows for a spatial splitting of the wave packets that can be, in principle, tested experimentally.

When the electric and sufficiently weak magnetic fields are perpendicular, the valley separation is negligible for the equal initial weights of the degenerate chirality states. On the other hand, the non-Abelian corrections lead to a well-pronounced oscillating motion of the wave packets in the direction parallel to the magnetic field. If detected, such deviations from the usual in-plane motion could provide another signature of the non-Abelian effects. In addition, there is also a weak chirality polarization of the states from different Dirac points, which, however, is not easily accessible because the trajectories from different valleys are not well-split. The situation changes at sufficiently large magnetic fields, when the trajectories from different valleys are separated along the direction of the magnetic field.

However, the separation is nonmonotonic and is estimated to be relatively weak. Therefore, while the case of the perpendicular electric and magnetic fields contains interesting physics, it might be difficult to realize experimentally.

It is instructive to compare the obtained results with those in Ref. [45], where the valley and chirality splitting was shown to be possible by applying a superposition of magnetic and strain-induced pseudomagnetic fields. In the absence of the chirality-mixing term $\Delta(\mathbf{k})$ and the non-Abelian corrections to the Berry curvature, however, it was critical to include a pseudomagnetic field. Without the latter, the right- and left-handed beams from different valleys would overlap and form nonchiral beams that do not correspond to a certain valley. In contrast, as we showed in the study here, the non-Abelian effects and the gap term can lead to both valley and chirality splittings even in the absence of a pseudomagnetic field. While the effects are estimated to be rather small, they can be experimentally accessible via certain local probes.

Acknowledgments

The work of E.V.G. was partially supported by the Program of Fundamental Research of the Physics and Astronomy Division of the National Academy of Sciences of Ukraine. The work of V.A.M. and P.O.S. was supported by the Natural Sciences and Engineering Research Council of Canada. The work of I.A.S. was supported by the U. S. National Science Foundation under Grants No. PHY-1404232 and No. PHY-1713950.

Appendix A: Explicit expressions for the Berry connection, the Berry curvature, and the magnetic moment

In this appendix, we present the explicit expressions for the Berry connection, the Berry curvature, and the magnetic moment defined in the main text by Eqs. (17), (18), and (20), respectively. Unfortunately, the general form of the corresponding results is bulky. Therefore, we consider only the linear in α approximation.

Let us start from the Berry connection $\mathbf{A}_{mn}^{(\pm)}$ given by Eq. (17). Here, the upper index corresponds to the linearized Hamiltonian given either by Eq. (7) or Eq. (8) in the main text and $n, m = \pm$ correspond to the wave functions defined in the main text by Eqs. (12) and (13), respectively. The explicit expressions for the Berry connection matrix components are

$$\mathbf{A}_{++}^{(\pm)} = \frac{(k \pm k_z)}{2k_{\perp}^2 k} \{-k_y, k_x, 0\}, \quad (\text{A1})$$

$$\mathbf{A}_{+-}^{(\pm)} = \frac{i\alpha(\sqrt{m} \pm k_z)k_-}{2v_F k_+ k_{\perp} k} \left\{ k_x k_z + 2ik_y(k_z \mp k), k_y k_z - 2ik_x(k_z \mp k), \pm \frac{k_{\perp}^2 k_z}{(\sqrt{m} \pm k_z)} \right\}, \quad (\text{A2})$$

$$\mathbf{A}_{-+}^{(\pm)} = \left(\mathbf{A}_{+-}^{(\pm)} \right)^{\dagger}, \quad (\text{A3})$$

$$\mathbf{A}_{--}^{(\pm)} = \frac{(k \mp k_z)}{2k_{\perp}^2 k} \{-k_y, k_x, 0\}, \quad (\text{A4})$$

where $k = \sqrt{k_{\perp}^2 + k_z^2}$, $k_{\perp} = \sqrt{k_x^2 + k_y^2}$, v_F is the Fermi velocity measured in the energy units, \sqrt{m} determines the separation of the Dirac points in the momentum space, and the parameter α defines the strength of the off-diagonal terms in Hamiltonians (7) and (8) in the main text. It is worth noting that the z component of the Berry connection matrix $\mathbf{A}_{nm}^{(\pm)}$ vanishes when the dependence on k_z is ignored in $\Delta(\mathbf{k})$.

Further, we present the results for the Berry curvature matrix $\Omega_{mn}^{(\pm)}$ given by Eq. (18) in the main text. Its

components are

$$\Omega_{++}^{(\pm)} = \mp \frac{\mathbf{k}}{2\hbar k^3}, \quad (\text{A5})$$

$$\begin{aligned} \Omega_{+-}^{(\pm)} = & \frac{\alpha k_-}{2v_F \hbar k_{\perp} k_{+} k^3} \left\{ -\sqrt{m} k_{\perp}^2 (2k_x + ik_y) \mp 2k_{\perp}^2 k_{+} k_z + k_x k (2k_{\perp}^2 + k_z^2), \right. \\ & - \sqrt{m} k_{\perp}^2 (2k_y - ik_x) \pm 2ik_{\perp}^2 k_{+} k_z + k_y k (2k_{\perp}^2 + k_z^2), \\ & \left. \mp (\sqrt{m} \pm k_z) \frac{2k_x^4 + 2k_y^4 + k_z^4 + k_y^2 k_z (3k_z \pm 2k) + k_x^2 [4k_y^2 + k_z (3k_z \pm 2k)]}{k} \right\}, \end{aligned} \quad (\text{A6})$$

$$\Omega_{-+}^{(\pm)} = \left(\Omega_{+-}^{(\pm)} \right)^{\dagger}, \quad (\text{A7})$$

$$\Omega_{--}^{(\pm)} = \pm \frac{\mathbf{k}}{2\hbar k^3}, \quad (\text{A8})$$

where \hbar is the Planck constant. Finally, the components of the magnetic moment matrix $\mathbf{M}_{mn}^{(\pm)}$ given by Eq. (20) in the main text read as

$$\mathbf{M}_{++}^{(\pm)} = \mp \frac{ev_F \mathbf{k}}{2\hbar ck^2} = \frac{ev_F k}{c} \Omega_{++}^{\pm}, \quad (\text{A9})$$

$$\begin{aligned} \mathbf{M}_{+-}^{(\pm)} = & \frac{e\alpha k_{\perp} k_{+}}{2\hbar ck_{+} k^2} \left\{ k_x [k - 2(\sqrt{m} \pm k_z)] - ik_y (\sqrt{m} \pm 2k_z), k_y [k - 2(\sqrt{m} \pm k_z)] + ik_x (\sqrt{m} \pm 2k_z), \right. \\ & \left. \mp (\sqrt{m} \pm k_z) (k \pm 2k_z) \right\}, \end{aligned} \quad (\text{A10})$$

$$\mathbf{M}_{-+}^{(\pm)} = \left(\mathbf{M}_{+-}^{(\pm)} \right)^{\dagger}, \quad (\text{A11})$$

$$\mathbf{M}_{--}^{(\pm)} = \pm \frac{ev_F \mathbf{k}}{2\hbar ck^2} = \frac{ev_F k}{c} \Omega_{--}^{\pm}. \quad (\text{A12})$$

Here, c denotes the speed of light and e is the absolute value of the electron charge.

-
- [1] Z. Wang, Y. Sun, X. Q. Chen, C. Franchini, G. Xu, H. Weng, X. Dai, and Z. Fang, Phys. Rev. B **85**, 195320 (2012).
 - [2] Z. Wang, H. Weng, Q. Wu, X. Dai, and Z. Fang, Phys. Rev. B **88**, 125427 (2013).
 - [3] S. Borisenko, Q. Gibson, D. Evtushinsky, V. Zabolotnyy, B. Buchner, and R. J. Cava, Phys. Rev. Lett. **113**, 027603 (2014).
 - [4] M. Neupane, S.-Y. Xu, R. Sankar, N. Alidoust, G. Bian, C. Liu, I. Belopolski, T.-R. Chang, H.-T. Jeng, H. Lin, A. Bansil, F. Chou, and M. Z. Hasan, Nature Commun. **5**, 3786 (2014).
 - [5] Z. K. Liu, B. Zhou, Y. Zhang, Z. J. Wang, H. M. Weng, D. Prabhakaran, S.-K. Mo, Z. X. Shen, Z. Fang, X. Dai, Z. Hussain, and Y. L. Chen, Science **343**, 864 (2014).
 - [6] X. Wan, A. M. Turner, A. Vishwanath, and S. Y. Savrasov, Phys. Rev. B **83**, 205101 (2011).
 - [7] C.-L. Zhang, Z. Yuan, Q.-D. Jiang, B. Tong, C. Zhang, X. C. Xie, and S. Jia Phys. Rev. B **95**, 085202 (2017).
 - [8] S.-Y. Xu, I. Belopolski, N. Alidoust, M. Neupane, C. Zhang, R. Sankar, S.-M. Huang, C.-C. Lee, G. Chang, B. Wang, G. Bian, H. Zheng, D. S. Sanchez, F. Chou, H. Lin, S. Jia, and M. Z. Hasan, Science **349**, 613 (2015).
 - [9] B. Q. Lv, H. M. Weng, B. B. Fu, X. P. Wang, H. Miao, J. Ma, P. Richard, X. C. Huang, L. X. Zhao, G. F. Chen, Z. Fang, X. Dai, T. Qian, and H. Ding, Phys. Rev. X **5**, 031013 (2015).
 - [10] X. Huang, L. Zhao, Y. Long, P. Wang, D. Chen, Z. Yang, H. Liang, M. Xue, H. Weng, Z. Fang, X. Dai, and G. Chen, Phys. Rev. X **5**, 031023 (2015).
 - [11] S.-Y. Xu, I. Belopolski, D. S. Sanchez, C. Zhang, G. Chang, C. Guo, G. Bian, Z. Yuan, H. Lu, T.-R. Chang, P. P. Shibayev, M. L. Prokopovych, N. Alidoust, H. Zheng, C.-C. Lee, S.-M. Huang, R. Sankar, F. Chou, C.-H. Hsu, H.-T. Jeng, *et al.*, Sci. Adv. **1**, e1501092 (2015).
 - [12] S.-Y. Xu, N. Alidoust, I. Belopolski, Z. Yuan, G. Bian, T.-R. Chang, H. Zheng, V. N. Strocov, D. S. Sanchez, G. Chang, C. Zhang, D. Mou, Y. Wu, L. Huang, C.-C. Lee, S.-M. Huang, B. Wang, A. Bansil, H.-T. Jeng, T. Neupert, A. Kaminski, H. Lin, S. Jia, and M. Z. Hasan, Nature Phys. **11**, 748 (2015).
 - [13] D.-F. Xu, Y.-P. Du, Z. Wang, Y.-P. Li, X.-H. Niu, Q. Yao, P. Dudin, Z.-A. Xu, X.-G. Wan, and D.-L. Feng, Chin. Phys. Lett. **32**, 107101 (2015).
 - [14] C. Shekhar, A. K. Nayak, Y. Sun, M. Schmidt, M. Nicklas, I. Leermakers, U. Zeitler, Y. Skourski, J. Wosnitza, Z. Liu, Y. Chen, W. Schnelle, H. Borrmann, Y. Grin, C. Felser, and B. Yan, Nat. Phys. **11**, 645 (2015).
 - [15] Z. Wang, Y. Zheng, Z. Shen, Y. Lu, H. Fang, F. Sheng, Y. Zhou, X. Yang, Y. Li, C. Feng, and Z.-A. Xu, Phys. Rev. B **93**, 121112(R) (2016).

- [16] C.-L. Zhang, S.-Y. Xu, I. Belopolski, Z. Yuan, Z. Lin, B. Tong, G. Bian, N. Alidoust, C.-C. Lee, S.-M. Huang, T.-R. Chang, G. Chang, C.-H. Hsu, H.-T. Jeng, M. Neupane, D. S. Sanchez, H. Zheng, J. Wang, H. Lin, C. Zhang, H.-Z. Lu, S.-Q. Shen, T. Neupert, M. Z. Hasan, and S. Jia, *Nat. Commun.* **7**, 10735 (2016).
- [17] M. Z. Hasan, S.-Y. Xu, I. Belopolski, and C.-M. Huang, *Ann. Rev. Cond. Mat. Phys.* **8**, 289 (2017).
- [18] B. Yan and C. Felser, *Ann. Rev. Cond. Mat. Phys.* **8**, 337 (2017).
- [19] N. P. Armitage, E. J. Mele, and A. Vishwanath, *Rev. Mod. Phys.* **90**, 15001 (2018).
- [20] M. V. Berry, *Proc. R. Soc. London Ser. A* **392**, 45 (1984).
- [21] H. B. Nielsen and M. Ninomiya, *Nucl. Phys. B* **185**, 20 (1981).
- [22] H. B. Nielsen and M. Ninomiya, *Nucl. Phys. B* **193**, 173 (1981).
- [23] V. Aji, *Phys. Rev. B* **85**, 241101 (2012).
- [24] F. D. M. Haldane, arXiv:1401.0529.
- [25] S.-Y. Xu, C. Liu, S. K. Kushwaha, R. Sankar, J. W. Krizan, I. Belopolski, M. Neupane, G. Bian, N. Alidoust, T.-R. Chang, H.-T. Jeng, C.-Y. Huang, W.-F. Tsai, H. Lin, P. P. Shibayev, F.-C. Chou, R. J. Cava, M.Z. Hasan, *Science* **347**, 294 (2015).
- [26] A. C. Potter, I. Kimchi, and A. Vishwanath *Nat. Commun.* **5**, 5161 (2014).
- [27] P. J. W. Moll, N. L. Nair, T. Helm, A. C. Potter, I. Kimchi, A. Vishwanath, and J. G. Analytis, *Nature* **535**, 266 (2016).
- [28] B.-J. Yang and N. Nagaosa, *Nat. Commun.* **5**, 4898 (2014).
- [29] E. V. Gorbar, V. A. Miransky, I. A. Shovkovy, and P. O. Sukhachov, *Phys. Rev. B* **91**, 121101 (2015).
- [30] E. V. Gorbar, V. A. Miransky, I. A. Shovkovy, and P. O. Sukhachov, *Phys. Rev. B* **91**, 235138 (2015).
- [31] B.-J. Yang, T. Morimoto, and A. Furusaki, *Phys. Rev. B* **92**, 165120 (2015).
- [32] C. Fang, Y. Chen, H.-Y. Kee, and L. Fu, *Phys. Rev. B* **92**, 081201 (2015).
- [33] S. Kobayashi and M. Sato, *Phys. Rev. Lett.* **115**, 187001 (2015).
- [34] A. A. Burkov and Y. B. Kim, *Phys. Rev. Lett.* **117**, 136602 (2016).
- [35] M. Rogatko and K. I. Wysokinski, arXiv:1804.02202.
- [36] F. Wilczek and A. Zee, *Phys. Rev. Lett.* **52**, 2111 (1984).
- [37] D. T. Son and N. Yamamoto, *Phys. Rev. Lett.* **109**, 181602 (2012).
- [38] M. A. Stephanov and Y. Yin, *Phys. Rev. Lett.* **109**, 162001 (2012).
- [39] J. Y. Chen, D. T. Son, M. A. Stephanov, H. U. Yee, and Y. Yin, *Phys. Rev. Lett.* **113**, 182302 (2014).
- [40] C. Manuel and J. M. Torres-Rincon, *Phys. Rev. D* **90**, 076007 (2014).
- [41] R. Shindou and K. I. Imura, *Nucl. Phys. B* **720**, 399 (2005).
- [42] D. Culcer, Y. Yao, and Q. Niu, *Phys. Rev. B* **72**, 085110 (2005).
- [43] M. C. Chang and Q. Niu, *J. Phys. Condens. Matter* **20**, 193202 (2008).
- [44] D. Xiao, M. C. Chang, and Q. Niu, *Rev. Mod. Phys.* **82**, 1959 (2010).
- [45] E. V. Gorbar, V. A. Miransky, I. A. Shovkovy, and P. O. Sukhachov, *Phys. Rev. B* **95**, 241114 (2017).
- [46] T. Liang, Q. Gibson, M. N. Ali, M. Liu, R. J. Cava, and N. P. Ong, *Nat. Mater.* **14**, 280 (2015).